Spontaneous separation and evaporation mechanism of self-rewetting fluid droplets on chemically stripe-patterned surfaces: A lattice Boltzmann study

Yue Yu, Zhuohui Yin, Qing Li,[*] and Shi Tang
School of Energy Science and Engineering, Central South University, Changsha 410083, People's Republic of China

(Received 14 July 2022; accepted 21 October 2022; published 10 November 2022)

The evaporation characteristics of self-rewetting fluids have attracted much attention in recent years. However, the evaporation dynamics as well as the underlying evaporation mechanism of self-rewetting fluid droplets has not been well understood. In this paper, we numerically investigate the evaporation performance and the dynamic behavior of self-rewetting fluid droplets on chemically patterned surfaces using a thermal multiphase lattice Boltzmann model with liquid-vapor phase change. First, it is shown that a self-rewetting fluid droplet can spontaneously separate into two droplets during its evaporation on a hydrophilic surface with a hydrophobic stripe, while no separation occurs during the evaporation of a conventional fluid droplet. The positive surface tension gradient of the self-rewetting fluid is found to play an important role in the spontaneous separation of the self-rewetting fluid droplet during the evaporation. Meanwhile, the separation behavior of the self-rewetting fluid droplet can effectively increase the length of the triple-phase contact line, which leads to a significant increase in the evaporation rate as compared with that of a conventional fluid droplet. Moreover, by investigating the evaporation performance of self-rewetting fluid droplets on chemically stripe-patterned surfaces with different values of the widths of the hydrophilic and hydrophobic stripes, it is found that the stripe width and the initial location of the droplet significantly affect the dynamic behavior and the evaporation efficiency of the self-rewetting fluid droplet. For different relative positions between the droplet and the stripes, the droplet may spontaneously separate into two or three droplets and achieve much better evaporation efficiency when the stripe width is within an optimal range.

DOI: 10.1103/PhysRevE.106.055104

I. INTRODUCTION

Droplet evaporation is a fundamental phenomenon in nature and plays a very important role in many industrial applications, such as coating [1], inkjet printing [2], desalination of sea water [3], and spray cooling [4]. Understanding the underlying physical mechanism of droplet evaporation and enhancing the evaporation efficiency are of great significance for these applications. Generally, the evaporation of droplets on a surface is significantly influenced by various factors [5], including the structure and the chemical composition of the surface, the physical properties of the working fluid [6–8], etc. Therefore, the design of the evaporation surface and the choice of the working fluid are very important for improving the evaporation heat transfer performance.

In the literature, some efforts have been made to understand the mechanism of droplet evaporation on chemically patterned surfaces, which showed that the droplet evaporation on a chemically patterned surface usually exhibits unique shape and droplet dynamics as compared with that on a homogeneous surface, such as irregular contact surfaces, pinning of contact lines, and indeterminate contact angles [9–12]. In 2009, Bliznyuk *et al.* [13] investigated the asymmetric glycerol droplet shapes on chemically patterned surfaces. The equilibrium shape as well as the unique scaling behavior of the contact angles was observed owing to the well-defined small droplet volume. Afterward, they presented experimental results on the spreading of glycerol droplets on chemically patterned surfaces [14] and found that the liquid was "pushed" in the direction parallel to the stripes. In addition, the "squeezing" mechanism of the droplet was observed. Following the study of Bliznyuk *et al.*, Jansen *et al.* [15] investigated the evaporation of droplets on a vertically stripe-patterned surface through experiments. It was found that the droplets were elongated on the vertically stripe-patterned surface, and the evaporation of the elongated droplets was faster than spherical droplets because the elongation plays an important role in the diffusion process, which leads to a reduction of the total evaporation time. Additionally, Li *et al.* [16] numerically investigated the pinning and depinning mechanism of the contact line during droplet evaporation on chemically stripe-patterned surfaces.

The aforementioned studies were focused on conventional fluids, for which the surface tension usually decreases with the increase of the temperature, leading to a negative surface tension gradient ($d\gamma/dT < 0$) and resulting in a surface flow that is directed from the region of lower surface tension (hot region) to the region of higher surface tension (cold region). In 2005, Abe *et al.* [17] carried out a pioneering study on self-rewetting fluids. In comparison with conventional fluids, the relationship between the surface tension and the temperature of self-rewetting fluids is nonlinear [18]. For self-rewetting fluids, the surface tension decreases with the increase of the

---

[*] Corresponding author: qingli@csu.edu.cn

©2022 American Physical Society

temperature when the temperature is lower than a critical value, and then increases when the temperature is higher than the critical value. The positive surface tension gradient ($d\gamma/dT > 0$) of self-rewetting fluids can induce an inverse-thermocapillary flow as compared with conventional fluids, i.e., a flow from the cold region to the hot region of the interface. The corresponding Marangoni convection is expected to overcome other forces to drive the cold liquid to the hot region [19]. Therefore, the evaporation performance and the dynamic properties of self-rewetting fluids are usually different from those of conventional fluids [20–22].

Some studies have been conducted on the evaporation of self-rewetting fluids. For instance, Lim *et al.* [23] investigated the inverse-thermocapillary effect in an evaporating thin liquid film of self-rewetting fluids. They demonstrated that the positive surface tension gradient of self-rewetting fluids induces the inverse-thermocapillary flow and found that the inverse-thermocapillary effect can enhance the evaporation rate. Yang *et al.* [24] studied the effects of self-rewetting fluids on the evaporation mode. They found that the self-rewetting fluids are conducive to increasing the microscopic critical contact angle and the energy barrier of the contact line, which reduces the rate of the thin-film thickness variation and affects the evaporation performance. Sefiane *et al.* [25] investigated the evaporation heat and mass transfer in open microchannels using self-rewetting fluids. The “contact angle shift” phenomenon of self-rewetting fluids was observed, which indicates a more efficient heat transfer process of a heated self-rewetting fluid meniscus.

Although the local changes at the triple-phase contact line during the evaporation of self-rewetting fluids have been observed in previous studies, little attention has been devoted to the dynamic behavior and the associated evaporation enhancement mechanism of self-rewetting fluid droplets during evaporation on chemically patterned surfaces. With the rapid development of computational technology, computational fluid dynamics (CFD) has become an important method for studying liquid-vapor phase change problems. Compared with experiments, numerical simulations can provide more details of the fluid dynamics during the phase change processes. In the past three decades, the lattice Boltzmann (LB) method has been developed into a very efficient and reliable numerical method [26–31], which has been widely used in the simulations of droplet evaporation. In order to carry out the numerical simulations of self-rewetting fluids, an important treatment is to tune the surface tension of the working fluids. In 2013, Li and Luo [32] proposed an efficient approach to tune the surface tension in the pseudopotential multiphase LB method [33], which is one of the most popular multiphase methods in the LB community. Subsequently, Xu *et al.* [34] and Fei *et al.* [35] extended Li and Luo’s approach to the three-dimensional (3D) space by using the D3Q15 and D3Q19 lattices, respectively.

In this work, by using a 3D thermal multiphase LB model based on the D3Q15 lattice [34], we aim at numerically investigating the evaporation performance of self-rewetting fluid droplets on chemically patterned surfaces, so as to provide an understanding of the dynamic behavior and the evaporation enhancement mechanism of self-rewetting fluid droplets on chemically patterned surfaces. The rest of the present paper is organized as follows. In Sec. II, a 3D thermal multiphase LB model with liquid-vapor phase change is introduced. Numerical investigation of the self-rewetting fluid droplet evaporation on chemically patterned surfaces is conducted in Sec. III, with a focus being placed on the spontaneous separation behavior of the self-wetting fluid droplets and the associated evaporation enhancement mechanism on chemically patterned surfaces. Finally, a brief summary is given in Sec. IV.

II. METHODOLOGY

Using a multiple-relaxation-time (MRT) collision operator, the LB equation, which governs the evolution of the density distribution function, can be written as follows:

$$f_\alpha(\mathbf{x}+\mathbf{e}_\alpha\delta_t, t+\delta_t) = f_\alpha(\mathbf{x},t) - \widehat{\Lambda}_{\alpha\beta}\left(f_\beta - f_\beta^{eq}\right)\big|_{(\mathbf{x},t)} + \delta_t F_\alpha(\mathbf{x},t), \tag{1}$$

where f_α is the density distribution function, f_α^{eq} is the equilibrium density distribution function, $\mathbf{x}$ is the spatial position, $\mathbf{e}_\alpha$ is the discrete velocity in the α th direction, t is the time, δ_t is the time step, F_α denotes the forcing term in the discrete velocity space, and $\widehat{\Lambda}_{\alpha\beta} = (\mathbf{M}^{-1}\mathbf{\Lambda}\mathbf{M})_{\alpha\beta}$ is the collision matrix, in which $\mathbf{M}$ is a transformation matrix and $\mathbf{\Lambda}$ is a diagonal relaxation matrix. Besides the MRT version, an entropic version [36] of the pseudopotential multiphase LB model has also been demonstrated to be capable of significantly enhancing its numerical stability at high Reynolds and Weber numbers.

The three-dimensional 15-velocity (D3Q15) lattice is adopted in the present work, i.e.,

$$\mathbf{e}_\alpha = c\begin{bmatrix} 0 & 1 & -1 & 0 & 0 & 0 & 0 & 1 & -1 & 1 & -1 & 1 & -1 & 1 & -1 \\ 0 & 0 & 0 & 1 & -1 & 0 & 0 & 1 & -1 & 1 & -1 & -1 & 1 & -1 & 1 \\ 0 & 0 & 0 & 0 & 0 & 1 & -1 & 1 & -1 & -1 & 1 & 1 & -1 & -1 & 1 \end{bmatrix}, \tag{2}$$

where $c = 1$ is the lattice constant. Correspondingly, the relaxation matrix is given by $\mathbf{\Lambda} = \mathrm{diag}(s_\rho, s_e, s_\varsigma, s_j, s_q, s_j, s_q, s_j, s_q, s_v, s_v, s_v, s_v, s_v, s_{xyz})$. The improved pseudopotential multiphase LB method with tunable surface tension proposed by Li and Luo [32] has been extended to the D3Q15 lattice by Xu *et al.* [34]. By multiplying Eq. (1) with the transformation matrix, the right-hand side of the LB equation can be rewritten as follows:

$$\mathbf{m}^* = \mathbf{m} - \mathbf{\Lambda}(\mathbf{m} - \mathbf{m}^{eq}) + \delta_t\left(\mathbf{I} - \frac{\mathbf{\Lambda}}{2}\right)\mathbf{S} + \delta_t\mathbf{C}, \tag{3}$$

where $\mathbf{m} = \mathbf{Mf}$ and the equilibria $\mathbf{m}^{eq}$ are given by

$$\mathbf{m}^{eq} = \rho\big(1, -1 + |\mathbf{v}|^2, 1 - 5|\mathbf{v}|^2, v_x, -\tfrac{7}{3}v_x, v_y, -\tfrac{7}{3}v_y, v_z, -\tfrac{7}{3}v_z, 2v_x^2 - v_y^2 - v_z^2, v_y^2 - v_z^2, v_xv_y, v_yv_z, v_xv_z, 0\big)^{\mathrm{T}}. \tag{4}$$

The forcing term $\mathbf{S}$ and the source term $\mathbf{C}$ are given by [34], respectively,

$$\mathbf{S} = \begin{bmatrix} 0 \\ 2\mathbf{v}\cdot\mathbf{F} + \frac{6\sigma_{\mathrm{c}}|\mathbf{F}|^2}{\psi^2\delta_t(s_e^{-1}-0.5)} \\ -10\mathbf{v}\cdot\mathbf{F} \\ F_x \\ -\tfrac{7}{3}F_x \\ F_y \\ -\tfrac{7}{3}F_y \\ F_z \\ -\tfrac{7}{3}F_z \\ 4v_xF_x - 2v_yF_y - 2v_zF_z \\ 2v_yF_y - 2v_zF_z \\ v_xF_y + v_yF_x \\ v_yF_z + v_zF_y \\ v_xF_z + v_zF_x \\ 0 \end{bmatrix},$$

$$\mathbf{C} = \begin{bmatrix} 0 \\ \tfrac{4}{5}s_e(Q_{xx} + Q_{yy} + Q_{zz}) \\ 0 \\ 0 \\ 0 \\ 0 \\ 0 \\ 0 \\ 0 \\ -s_v(2Q_{xx} - Q_{yy} - Q_{zz}) \\ -s_v(Q_{yy} - Q_{zz}) \\ -s_vQ_{xy} \\ -s_vQ_{yz} \\ -s_vQ_{xz} \\ 0 \end{bmatrix}, \tag{5}$$

where the variables Q_{xx}, Q_{xy}, Q_{xz}, Q_{yy}, Q_{yz}, and Q_{xz} are calculated by

$$\boldsymbol{Q} = \sigma_\kappa \frac{G}{2}\psi(\mathbf{x}) \sum_{\alpha=1}^{14} \omega_\alpha[\psi(\mathbf{x} + \mathbf{e}_\alpha\delta_t) - \psi(\mathbf{x})]\mathbf{e}_\alpha\mathbf{e}_\alpha, \tag{6}$$

where $\psi(\mathbf{x})$ is the pseudopotential and the parameter σ_κ is used to tune the surface tension. The macroscopic density and velocity are defined as, respectively,

$$\rho = \sum_\alpha f_\alpha, \quad \rho\mathbf{v} = \sum_\alpha \mathbf{e}_\alpha f_\alpha + \frac{\delta_t}{2}\mathbf{F}, \tag{7}$$

where $\mathbf{F}$ is the force exerted on the system. For single-component multiphase flows, the interaction force in the pseudopotential multiphase LB method can be expressed as follows:

$$\mathbf{F} = -G\psi(\mathbf{x}) \sum_{\alpha=1}^{14} \omega_\alpha \psi(\mathbf{x} + \mathbf{e}_\alpha\delta_t)\mathbf{e}_\alpha, \tag{8}$$

where G is the interaction strength and ω_α are the weights, which are given by $\omega_{1-6} = 1/3$ and $\omega_{7-14} = 1/24$. As seen from Eq. (8), in the present work the standard stencil is utilized for the pseudopotential interaction force. Here it is worth mentioning that one can also employ a more isotropic stencil [37,38], which can reduce the spurious currents around the phase interfaces in the cases of multiphase flows at large density ratios.

By employing the Chapman-Enskog multiscale analysis, it can be found that the aforementioned pseudopotential multiphase LB model recovers the following macroscopic equations [34]:

$$\frac{\partial\rho}{\partial t} + \nabla\cdot(\rho\mathbf{v}) = 0, \tag{9}$$

$$\frac{\partial(\rho\mathbf{v})}{\partial t} + \nabla\cdot(\rho\mathbf{v}\mathbf{v}) = -\nabla\cdot\mathbf{P} + \nabla\cdot\mathbf{\Pi}, \tag{10}$$

where $\mathbf{\Pi}$ is the viscous stress tensor and $\mathbf{P}$ is the pressure tensor; they are given, respectively, by [34]

$$\mathbf{\Pi} = \rho\nu[\nabla\mathbf{v} + (\nabla\mathbf{v})^{\mathrm{T}}] + \rho\left(\xi - \frac{2}{3}\nu\right)(\nabla\cdot\mathbf{v})\mathbf{I}, \tag{11}$$

$$\mathbf{P} = \left[\rho c_s^2 + \frac{Gc^2}{2}\psi^2 + \frac{Gc^4}{12}(1 + 2\sigma_\kappa)\psi\nabla^2\psi + 2\sigma_{\mathrm{c}}G^2c^4|\nabla\psi|^2\right]\mathbf{I} + (1 - \sigma_\kappa)\frac{Gc^4}{6}\psi\nabla\nabla\psi, \tag{12}$$

where ν is the kinematic shear viscosity, ξ is the bulk viscosity, $\mathbf{I}$ is the unit tensor, and $c_s = c/\sqrt{3}$ is the lattice sound speed. The last term on the right-hand side of Eq. (12) determines the surface tension.

The pseudopotential $\psi(\mathbf{x})$ plays an important role in the pseudopotential multiphase LB method and can be taken as $\psi(\mathbf{x}) = \sqrt{2(P_{\mathrm{EOS}} - \rho c_s^2)/Gc^2}$ [33], where P_{EOS} is a nonideal equation of state. In the present work, we utilize the Peng-Robinson equation of state, i.e.,

$$p_{\mathrm{EOS}} = \frac{\rho RT}{1 - b\rho} - \frac{\alpha\varphi(T)\rho^2}{1 + 2b\rho - b^2\rho^2}, \tag{13}$$

$$\varphi(T) = [1 + (0.374\,64 + 1.542\,26\omega - 0.269\,92\omega^2) \times (1 - \sqrt{T/T_c})]^2, \tag{14}$$

where $a = 0.457\,24R^2T_c^2/\rho_c$ and $b = 0.0778RT_c/\rho_c$. The parameter $\omega = 0.344$ is the acentric factor and T_c is the critical temperature. According to Ref. [33] and the relationship between a and the interface thickness, in the present LB simulations we choose $a = 3/49$, $b = 2/21$, and $R = 1$.

The temperature equation can be derived from the local balance law for entropy. For nonideal fluids, by neglecting the viscous heat dissipation, the governing equation for the temperature field is given by

$$\partial_t T = -\mathbf{v}\cdot\nabla T + \frac{1}{\rho c_V}\nabla\cdot(\lambda\nabla T) - \frac{T}{\rho c_V}\left(\frac{\partial p_{\mathrm{EOS}}}{\partial T}\right)\nabla\cdot\mathbf{v}, \tag{15}$$

where λ is the thermal conductivity and c_V is the specific heat at constant volume. The second-order Runge-Kutta scheme

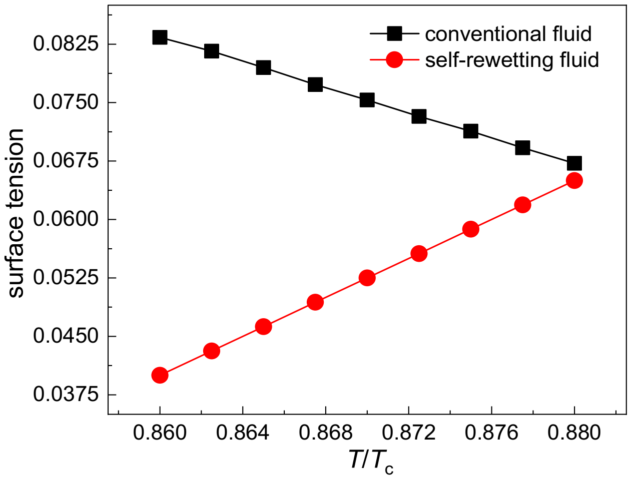

FIG. 1. The simulated surface tension (in lattice units) for a conventional fluid and a self-rewetting fluid, respectively.

is employed to solve Eq. (15). The isotropic central schemes are applied for the spatial discretization. For a quantity ϕ, the spatial gradient of ϕ and the Laplacian of ϕ are evaluated by the following second-order isotropic difference schemes, respectively,

$$\partial_i \phi(\mathbf{x}) \approx \frac{1}{c_s^2 \delta_t} \sum_\alpha w_\alpha \phi(\mathbf{x} + \mathbf{e}_\alpha \delta_t) e_{\alpha i}, \tag{16}$$

$$\nabla^2 \phi(\mathbf{x}) \approx \frac{2}{c_s^2 \delta_t^2} \sum_\alpha w_\alpha [\phi(\mathbf{x} + \mathbf{e}_\alpha \delta_t) - \phi(\mathbf{x})], \tag{17}$$

where $c_s = c/\sqrt{3}$ is the lattice sound speed. The weights w_α are given by $w_{1-6} = 1/9$ and $w_{7-14} = 1/72$. The capability of this 3D thermal multiphase LB model for simulating liquid-vapor phase change has been numerically validated in Ref. [11] by testing the well-known D^2 law for droplet vaporization.

In the present study, the saturation temperature is taken as $T_{\text{sat}} = 0.86T_c$, which corresponds to the liquid density $\rho_L \approx 6.5$ and the vapor density $\rho_V \approx 0.38$. All the quantities are taken in lattice units (l.u.), i.e., the units of the LB method, which are based on the lattice constant $c = \delta_x/\delta_t = 1$. Using the above thermal LB model, a conventional fluid can be simulated by directly taking the parameter σ_κ in Eq. (6) as $\sigma_\kappa = 0$; the results are shown in Fig. 1. From the figure it can be seen that when $\sigma_\kappa = 0$ the simulated surface tension for the conventional fluid decreases with increasing the temperature. To mimic the surface tension variation of a self-rewetting fluid, the parameter σ_κ in Eq. (6) should vary with the temperature. Specifically, for the self-rewetting fluid, the simulated surface tension is taken as 0.04 in lattice units at T_{sat} and 0.065 at $0.88T_c$. In addition, it is assumed that the surface tension of the self-rewetting fluid follows a linear distribution between T_{sat} and $0.88T_c$, as shown in Fig. 1. In other words, for the simulated self-rewetting fluid, the surface tension increases linearly with the increase of the temperature. The trumpet-shape arrangement adopted in Fig. 1 for the surface tension distributions of the conventional fluid and the self-rewetting fluid is mainly based on the experimental observation in Ref. [39].

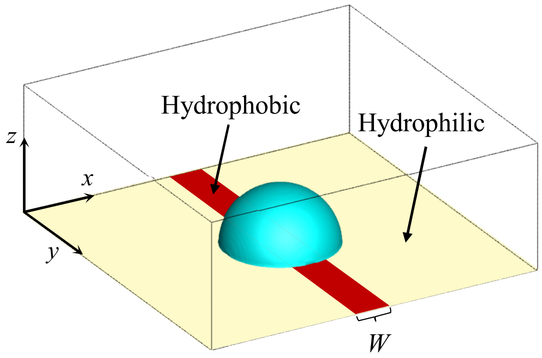

FIG. 2. Schematic overview of a droplet placed on a hydrophilic surface with a hydrophobic stripe.

III. NUMERICAL RESULTS AND DISCUSSION

A. Spontaneous separation of a self-rewetting fluid droplet during its evaporation on a hydrophilic surface with a hydrophobic stripe

In this section, the evaporation behaviors of self-rewetting fluid and conventional fluid droplets on a hydrophilic surface with a hydrophobic stripe are numerically investigated. The sketch of the evaporation surface is shown in Fig. 2, where the red stripe is hydrophobic but other regions are hydrophilic. The contact angles of the hydrophilic and hydrophobic regions are chosen as $\theta_{\text{phi}} \approx 50^\circ$ and $\theta_{\text{pho}} \approx 130^\circ$, respectively. Our simulations are performed in a rectangular domain $L_x \times L_y \times L_z = 160 \times 160 \times 61\,\text{l.u.}^3$. In simulations of this section, the width of the hydrophobic stripe is fixed at $W = 20\,\text{l.u.}$ The kinematic shear viscosity is taken as $\nu = 0.1$ and the specific heat at constant volume is set to $c_V = 2.0$ [11]. The nonslip boundary condition is applied at the bottom surface (the solid wall). The open boundary condition is used at the top boundary and the periodic boundary condition is employed in the x and y directions.

At the initial time step, a hemisphere droplet with a diameter of $d_0 = 50\,\text{l.u.}$ is placed on the center of the heating surface and the center of the droplet is located at the middle of the hydrophobic stripe. The initial temperature of the computational domain is taken as T_{sat}. The bottom of the domain is the heating surface and its temperature is given by $T_{\text{b}} = T_{\text{sat}} + \Delta T$, in which the wall superheat is taken as $\Delta T = 0.02T_c$.

The dynamic behavior of a self-rewetting fluid droplet during its evaporation on the hydrophilic surface with a hydrophobic stripe is displayed in Fig. 3. To quantify the numerical results, we have measured the contact length between the droplet and the heating surface in the middle x-z cross section and the contact length between the droplet and the hydrophobic stripe in the middle y-z cross section; they are denoted by D_x and D_y in Fig. 3(a), respectively. The measured results are shown in Fig. 4. At the initial state, a hemisphere droplet is placed on the heating surface with the contact angle of 90°, which is larger than $\theta_{\text{phi}} \approx 50^\circ$ but smaller than $\theta_{\text{pho}} \approx 130^\circ$. Hence, the contact line sitting on the hydrophobic stripe generates an unbalanced Young's force toward the center of the droplet, while the contact line sitting on the hydrophilic region yields an unbalanced Young's force

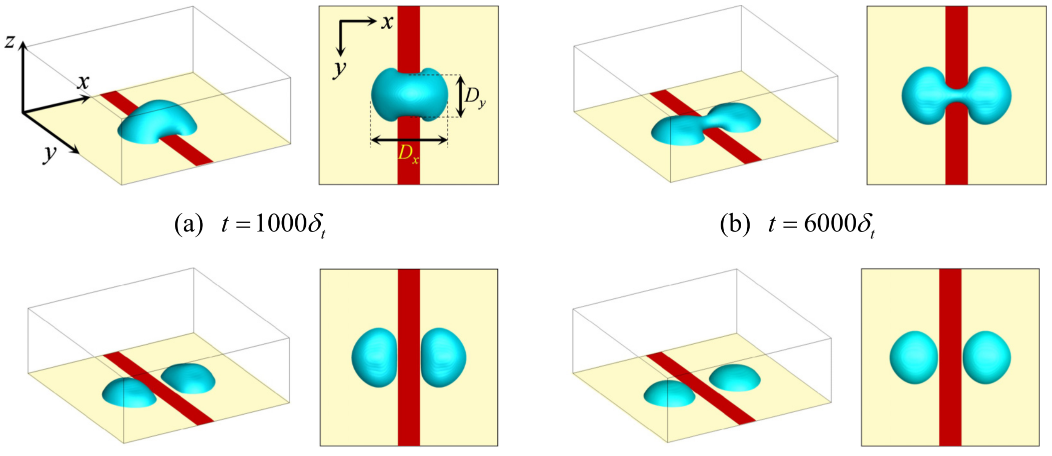

(a) $t = 1000\delta_t$ (b) $t = 6000\delta_t$

(c) $t = 7000\delta_t$ (d) $t = 10\,000\delta_t$

FIG. 3. 3D and vertical views of a self-rewetting fluid droplet during its evaporation on the hydrophilic surface with a hydrophobic stripe. (a) $t = 1000\delta_t$, (b) $6000\delta_t$, (c) $7000\delta_t$, and (d) $10\,000\delta_t$.

toward the outside. As a result, the droplet would spread on the hydrophilic region of the surface, but shrink on the hydrophobic stripe, which can be seen by comparing Fig. 3(a) with the initial droplet state in Fig. 2. Meanwhile, a liquid bridge is formed in the middle of the droplet and gradually gets narrower during the evaporation, as shown in Fig. 3(b). Correspondingly, the length of the triple-phase contact line is significantly increased as compared with that in Fig. 3(a), which can be seen from the vertical views provided in these two figures. The elongation of the triple-phase contact line is beneficial to enhancing the droplet evaporation and increasing the evaporation rate. We refer to the aforementioned stage as stage I of the whole evaporation process. For such a stage, from Fig. 4 we can see that the contact length D_x increases and the contact length D_y decreases due to the droplet spreading and shrinking on the hydrophilic and hydrophobic regions, respectively.

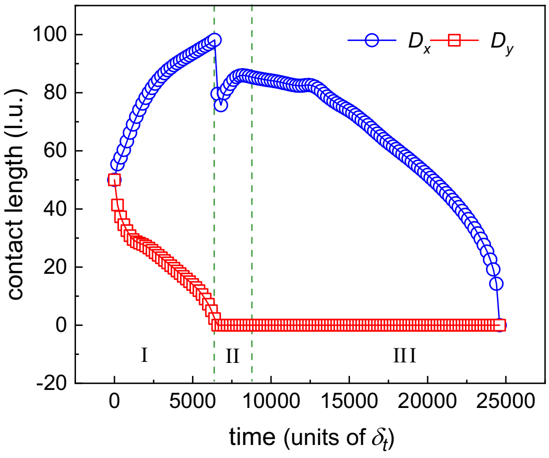

FIG. 4. Variations of the contact lengths D_x and D_y [see Fig. 3(a) for definitions] with time during the evaporation of a self-rewetting fluid droplet on the hydrophilic surface with a hydrophobic stripe.

Furthermore, stage II starts when the self-rewetting fluid droplet spontaneously separates into two small droplets, which occurs as the liquid bridge breaks at $t \approx 6400\delta_t$. Correspondingly, the contact length D_y is rapidly decreased to zero, as seen in Fig. 4, and there is a sudden decrease of D_x due to the breakup of the liquid bridge, which can also be observed by comparing Fig. 3(c) with Fig. 3(b). After the droplet separation, the two small droplets spread on the hydrophilic regions, which leads to an increase of the length of the triple-phase contact line and an increase of D_x in stage II, as shown in Fig. 4. Later, in stage III the two small droplets gradually evaporate with the triple-phase contact lines moving toward the center of each droplet. Accordingly, the contact length D_x, which consists of two parts after the droplet separation, is gradually decreased, as shown in Fig. 4.

For comparison, Fig. 5 displays the evaporation process of a conventional fluid droplet on the hydrophilic surface with a hydrophobic stripe. By comparing Fig. 5(a) with Fig. 3(a), we can see that in the early stage of the evaporation process ($t = 1000\delta_t$), the shape of the conventional fluid droplet is similar to that of the self-rewetting fluid droplet, which is expected since in the early stage the droplet has not been significantly heated by the bottom surface. However, as time goes by, obvious differences can be observed between the evaporation behavior of the conventional fluid droplet and that of the self-rewetting fluid droplet. Particularly, the major difference lies in that the self-rewetting fluid droplet can spontaneously separate into two small droplets, while the conventional fluid droplet cannot achieve spontaneous separation during the evaporation, as seen in Figs. 5(b)–5(d).

Owing to the spontaneous separation during the evaporation, the self-rewetting fluid droplet has a much longer triple-phase contact line than the conventional fluid droplet. For example, Figs. 3(d) and 5(b) provide the snapshots at the same time step and it is obvious that the triple-phase contact line in Fig. 3(d) is much longer than that in Fig. 5(b). The elongation of the triple-phase contact line can effectively increase the evaporation rate and reduce the total evaporation

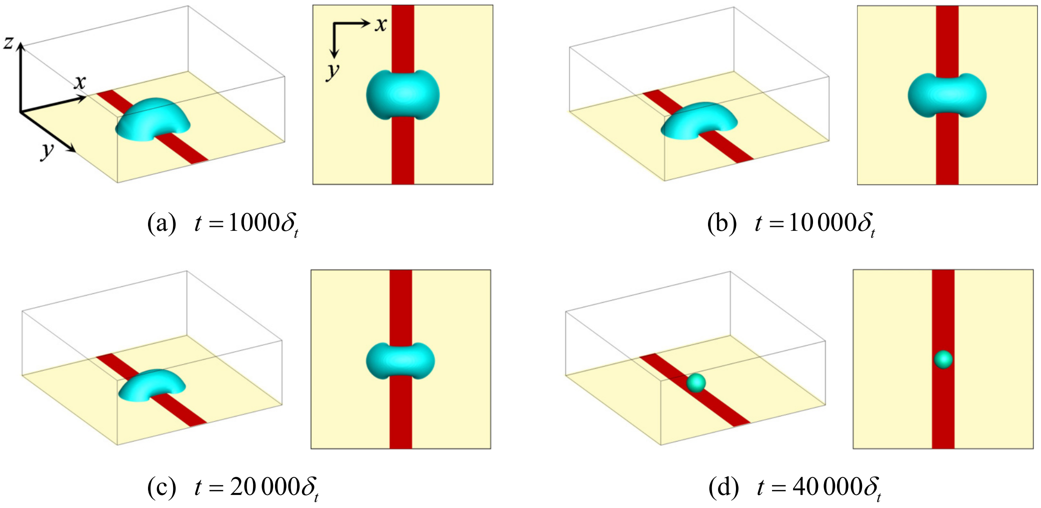

(a) $t = 1000\delta_t$

(b) $t = 10\,000\delta_t$

(c) $t = 20\,000\delta_t$

(d) $t = 40\,000\delta_t$

FIG. 5. 3D and vertical views of a conventional fluid droplet during its evaporation on the hydrophilic surface with a hydrophobic stripe. (a) $t = 1000\delta_t$, (b) $10\,000\delta_t$, (c) $20\,000\delta_t$, and (d) $40\,000\delta_t$.

time. Figure 6 shows the variations of the nondimensional droplet volume with time during the evaporation processes of the self-rewetting fluid droplet and the conventional fluid droplet on the hydrophilic surface with a hydrophobic stripe. As seen in the figure, the evaporation of the self-rewetting fluid droplet is much faster than that of the conventional fluid droplet. Quantitatively, the maximum evaporation rate of the self-rewetting fluid droplet is about twice that of the conventional fluid droplet and therefore the evaporation time of the self-rewetting fluid droplet is about one-half of that of the conventional fluid droplet.

Actually, according to the aforementioned numerical results, we can find that the spontaneous separation of the self-rewetting fluid droplet during the evaporation is mainly caused by two factors, i.e., the spreading of the droplet on the hydrophilic region and the shrinking of the droplet on the hydrophobic stripe. In the remainder of this section, we shall explain how the spontaneous separation occurs during the evaporation of the self-rewetting fluid droplet on the hydrophilic surface with a hydrophobic stripe. Figure 7 gives the schematic diagrams of the variations of the surface tension during the evaporation of a self-rewetting fluid droplet and a conventional fluid droplet on a uniformly hydrophobic surface, respectively. Specifically, Fig. 7(a) depicts the equilibrium state of a droplet on the uniformly hydrophobic surface under the isothermal condition without heating, in which θ_{e} is the intrinsic contact angle of the hydrophobic surface. Point A in Fig. 7(a), which is a point located at the liquid-vapor interface and close to the bottom surface, is selected as a typical point for analyzing the variation of the surface tension. Moreover, $\mathbf{F}_{\mathrm{a}}$ in Fig. 7(a) is the surface tension exerted by the liquid above point A, which is parallel to the liquid-vapor interface [40]. Similarly, $\mathbf{F}_{\mathrm{d}}$ is the surface tension exerted by the liquid below point A and the direction of $\mathbf{F}_{\mathrm{d}}$ is opposite to that of $\mathbf{F}_{\mathrm{a}}$, as shown in Fig. 7(a). When the droplet reaches its equilibrium state on the surface under the isothermal condition, $\mathbf{F}_{\mathrm{a}}$ and $\mathbf{F}_{\mathrm{d}}$ are equal in magnitude but opposite in direction.

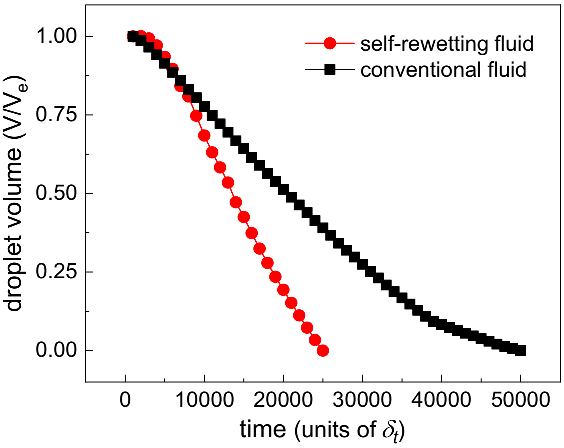

FIG. 6. Variations of the nondimensional droplet volume with time during the evaporation processes of the self-rewetting fluid droplet and the conventional fluid droplet on the hydrophilic surface with a hydrophobic stripe.

After heating, the positive surface tension gradient ($d\gamma/dT > 0$) of the self-rewetting fluid and the negative surface tension gradient ($d\gamma/dT < 0$) of the conventional fluid will lead to different variations of the surface tension, as shown in Figs. 7(b) and 7(d) for the self-rewetting fluid and conventional fluid droplets, respectively. For the self-rewetting droplet, after heating, the temperature of the liquid below point A is higher than that of the liquid above point A. As a result, $\mathbf{F}_{\mathrm{d}}$ is gradually larger than $\mathbf{F}_{\mathrm{a}}$ since the surface tension of the self-rewetting fluid increases with increasing the temperature. Accordingly, the component of the resultant force in the x direction points to the inside of the self-rewetting fluid droplet so that point A moves toward the center of the droplet, which causes the droplet to be deformed from the spherical shape, as illustrated in Fig. 7(c). After the droplet deformation, the dynamic contact angle (θ_{d}) is smaller than the intrinsic contact angle of the hydrophobic surface. Therefore, at the triple-phase contact line there should exist an unbalanced Young's force $\mathbf{F}_{\mathrm{u}} = \gamma(\cos\theta_{\mathrm{d}} - \cos\theta_{\mathrm{e}})$ (per unit

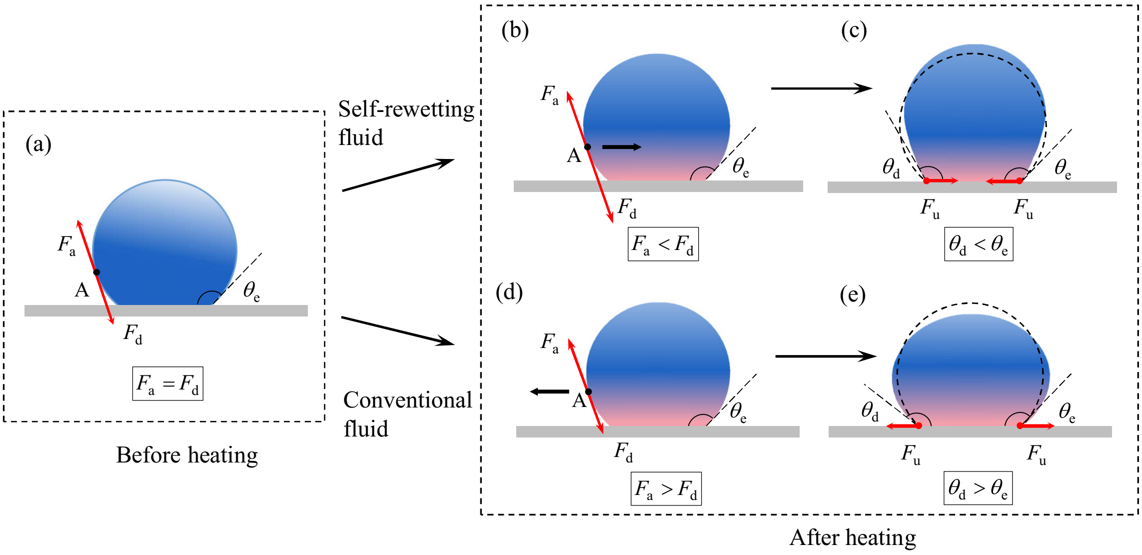

FIG. 7. Schematic diagrams of the variations of the surface tension during the evaporation of a self-rewetting fluid droplet and a conventional fluid droplet on a uniformly hydrophobic surface, respectively.

length) that it is oriented in the direction of the liquid phase, as shown in Fig. 7(c). As a consequence, the triple-phase contact line will move toward the center of the droplet so that the contact line will shrink on the hydrophobic surface during the evaporation.

However, for the conventional fluid droplet, after heating, the surface tension $\mathbf{F}_d$ gradually becomes smaller than $\mathbf{F}_a$ when the temperature increases, as illustrated in Fig. 7(d). Therefore, the component of the resultant force in the x direction points to the outside of the conventional fluid droplet so that the dynamic contact angle θ_d becomes larger than the intrinsic contact angle θ_e, which yields an unbalanced Young's force $\mathbf{F}_u$ toward the outside of the conventional fluid droplet, as shown in Fig. 7(e). Consequently, the triple-phase contact line moves toward the outside of the droplet and the conventional fluid droplet spreads on the hydrophobic surface.

Moreover, Fig. 8 displays the schematic diagrams of the variations of the surface tension during the evaporation of a self-rewetting fluid droplet and a conventional fluid droplet on a uniformly hydrophilic surface, respectively. Similar to Fig. 7(a), Fig. 8(a) also shows that $\mathbf{F}_a$ and $\mathbf{F}_d$ are equal in magnitude but opposite in direction under the isothermal condition. After heating, as shown in Fig. 8(b), the self-rewetting fluid droplet $\mathbf{F}_d$ is gradually larger than $\mathbf{F}_a$ with the increase of the temperature. Hence, the component of the resultant force in the x direction points to the outside of the self-rewetting fluid droplet so that point A moves in the direction of the outside of the droplet. Correspondingly, as shown in Fig. 8(c), the dynamic contact angle θ_d is larger than the intrinsic contact angle θ_e of the hydrophilic surface, which leads to an unbalanced Young's force $\mathbf{F}_u$ toward the outside of the droplet. As a consequence, the triple-phase contact line moves toward the outside of the droplet, which causes the self-rewetting fluid droplet to spread on the hydrophilic surface. In contrast, for the conventional fluid droplet, as shown in Fig. 8(d), the component of the resultant force in the x direction points to the inside of the conventional fluid droplet, which makes the dynamic contact angle θ_d smaller than the intrinsic contact angle θ_e. Therefore the unbalanced Young's force $\mathbf{F}_u$ points to the inside of the droplet and the triple-phase contact line shrinks on the hydrophilic surface, as shown in Fig. 8(e).

By comparing Fig. 8 with Fig. 7, some differences can be observed. The change in the dynamic contact angle caused by the positive surface tension gradient of the self-rewetting fluid results in a favorable unbalanced Young's force, which not only promotes the spreading of the self-rewetting fluid droplet on the hydrophilic surface but also promotes the shrinking of the self-rewetting fluid droplet on the hydrophobic surface. However, for the conventional fluid droplet, the change in the dynamic contact angle caused by the negative surface tension gradient leads to an unfavorable unbalanced Young's force, which is not conducive to the spreading of the droplet on the hydrophilic surface and the shrinking on the hydrophobic surface. In other words, during the evaporation on the aforementioned hydrophilic surface with a hydrophobic stripe, the positive surface tension gradient of the self-rewetting fluid droplet promotes its shrinking on the hydrophobic stripe and its spreading on the hydrophilic region, which consequently causes the spontaneous separation of the self-rewetting fluid droplet during the evaporation on the hydrophilic surface with a hydrophobic stripe. Conversely, the negative surface tension gradient of the conventional fluid droplet prevents it from shrinking on the hydrophobic stripe and spreading on the hydrophilic region, which suppresses the appearance of the spontaneous separation.

B. Evaporation performance and dynamic behavior of self-rewetting fluid droplets on chemically patterned surfaces when the droplet center is located at the middle of a hydrophobic stripe

In this section, the evaporation performance and the dynamic behavior of self-rewetting fluid droplets during the evaporation on chemically stripe-patterned surfaces are

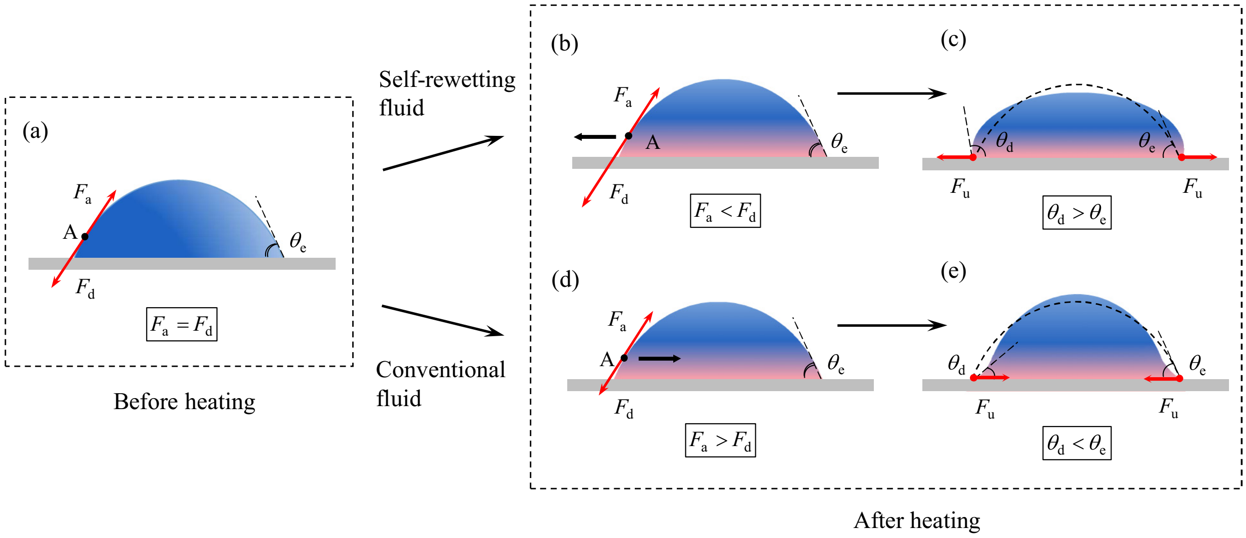

FIG. 8. Schematic diagrams of the variations of the surface tension during the evaporation of a self-rewetting fluid droplet and a conventional fluid droplet on a uniformly hydrophilic surface, respectively.

numerically investigated. The chemically heterogeneous surfaces patterned with hydrophilic and hydrophobic stripes are illustrated in Fig. 9, where the red stripes are hydrophobic while the yellow stripes are hydrophilic. The contact angles of the hydrophilic and hydrophobic stripes are chosen as $\theta_{\mathrm{phi}} \approx 50^\circ$ and $\theta_{\mathrm{pho}} \approx 130^\circ$, respectively. In addition, in this section we investigate the cases in which the droplet center is located at the middle of a hydrophobic stripe (see Fig. 9). At the initial state, a hemisphere droplet with a diameter of $d_0 = 50$ l.u. is placed at the center of the bottom surface. The widths of the hydrophilic and hydrophobic stripes are denoted by W_{phi} and W_{pho}, respectively. All other simulation parameters and the boundary conditions are the same as those used in the previous section. Also, to ensure the periodicity of the chemically stripe-patterned surfaces, L_x is adjusted according to the values of W_{phi} and W_{pho}. Furthermore, to show the details of the droplet dynamic behavior more clearly, the displayed domain is chosen as $N_x \times N_y \times N_z = 2.4d_0 \times 2.4d_0 \times 1.2d_0$ with the droplet being located at the center of the displayed domain.

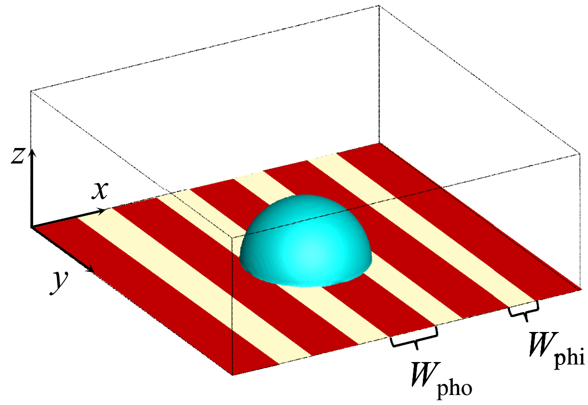

FIG. 9. Schematic overview of a droplet placed on a chemically stripe-patterned surface with the droplet center being located at the middle of a hydrophobic stripe.

Figure 10 shows the variations of the normalized evaporation time t_e^* of the self-rewetting fluid droplet with the normalized hydrophilic stripe width W_{phi}^* when the normalized hydrophobic stripe width is taken as $W_{\mathrm{pho}}^* = 0.12$, 0.4, and 0.72, respectively. The normalized evaporation time is defined as $t_e^* = t_e/t_{\mathrm{phi}}$, where t_e is the total evaporation time of the self-rewetting fluid droplet on a chemically stripe-patterned surface and t_{phi} is the total evaporation time of the self-rewetting fluid droplet on a uniformly hydrophilic surface whose intrinsic contact angle is $\theta_{\mathrm{phi}} \approx 50^\circ$. The normalized hydrophilic stripe width W_{phi}^* is defined as the ratio of the hydrophilic stripe width W_{phi} to the initial droplet diameter d_0. Similarly, the normalized hydrophobic stripe width W_{pho}^* denotes the ratio of the hydrophobic stripe width W_{pho} to the initial droplet diameter d_0. As shown in Fig. 10, the variation of the normalized evaporation time with the hydrophilic stripe width exhibits a similar trend under the three different widths of the hydrophobic stripes. To be specific, the normalized evaporation time t_e^* first decreases rapidly with the increase of the normalized hydrophilic stripe W_{phi}^* and then achieves a relatively stable development after reaching its minimum value, which corresponds to an optimal chemically stripe-patterned surface that can provide the fastest evaporation for the self-rewetting fluid droplet. For example, when W_{pho}^* is taken as 0.4, the minimum evaporation time and the fastest evaporation is achieved in the case of $W_{\mathrm{phi}}^* = 0.6$.

Figure 11(a) displays some snapshots during the evaporation of the self-rewetting fluid droplet in the case of $W_{\mathrm{pho}}^* = 0.12$ and $W_{\mathrm{phi}}^* = 0.12$. For this case, there is no droplet separation due to the fact that the widths of the hydrophobic and hydrophilic stripes are much smaller than the initial droplet diameter d_0. Under such a condition, the self-rewetting fluid droplet shares similar evaporation dynamics with a conventional fluid droplet [9,10,13–15]. The typical pinning-depinning or stick-slip phenomenon of the contact lines is also observed in this study. Besides, from Fig. 10(a) it can be found that for the case of $W_{\mathrm{pho}}^* = 0.12$ and $W_{\mathrm{phi}}^* = 0.12$ the normalized evaporation time t_e^* is about 1.52, indicating that

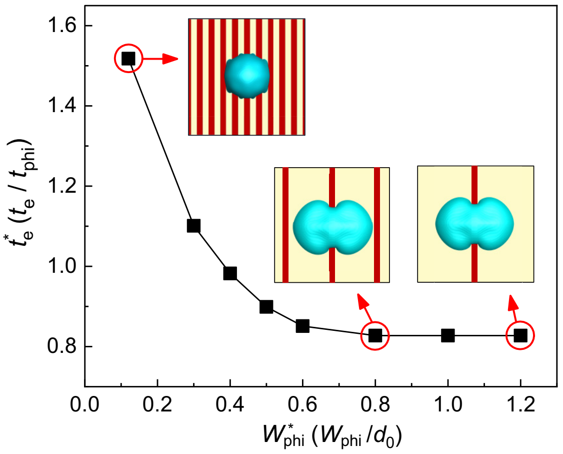

(a) $W_{pho}^* = 0.12$

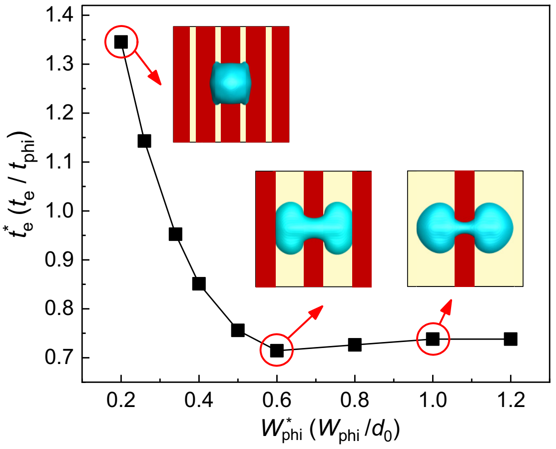

(b) $W_{pho}^* = 0.4$

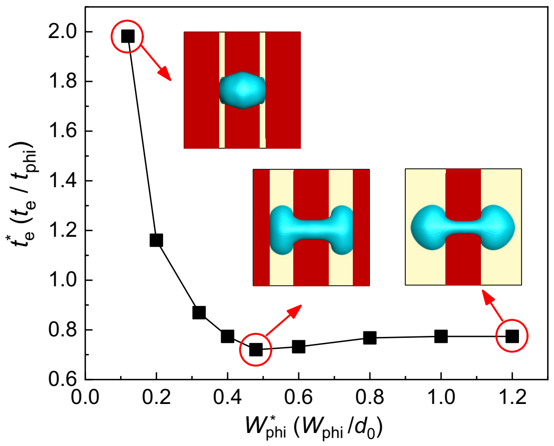

(c) $W_{pho}^* = 0.72$

FIG. 10. Variations of the normalized evaporation time t_e^* with the normalized hydrophilic stripe width W_{phi}^* when the normalized hydrophobic stripe width is taken as $W_{pho}^* = 0.12$, 0.4, and 0.72, respectively. The snapshots shown in this figure are taken at $t = 6000\delta_t$.

the evaporation of the self-rewetting fluid droplet in this case is much slower than that on a uniformly hydrophilic surface, which is expected since the self-rewetting fluid droplet mainly spreads on the hydrophilic stripes and the narrow hydrophilic stripes cannot provide enough space for the spreading of the droplet.

Figure 11(b) shows some snapshots of the droplet evaporation on the chemically stripe-patterned surface in the case of $W_{pho}^* = 0.12$ and $W_{phi}^* = 0.8$. In comparison with Fig. 11(a), in Fig. 11(b) the spreading space of the droplet on the hydrophilic stripes is considerably increased, which leads to a significant increase in the contact line length of the self-rewetting fluid droplet during the evaporation. Meanwhile, the spontaneous separation phenomenon of the self-rewetting fluid droplet is observed in this case, which occurs at $t \approx 240\,00\delta_t$. For this case, the normalized evaporation time t_e^* is around 0.8, as seen in Fig. 10(a), which implies that the evaporation rate of the self-rewetting droplet on the chemically stripe-patterned surface is significantly enhanced compared with that on a uniformly hydrophilic surface, as the elongation of the triple-phase contact line and the spontaneous separation of the droplet can enhance the evaporation heat transfer. When $W_{phi}^* > 0.8$, the normalized evaporation time of the droplet is almost unchanged [see Fig. 10(a)] because the hydrophobic stripes on both sides of the droplet have no effect on the droplet spreading when the width of the hydrophilic stripes is relatively large.

As the normalized hydrophobic stripe width is increased to $W_{pho}^* = 0.4$, different dynamic behaviors can be observed during the evaporation of the self-rewetting fluid droplet, as shown in Fig. 10(b). To further illustrate the influences of the hydrophilic stripe width on the evaporation performance and the dynamic behavior of the self-rewetting fluid droplet, some snapshots of the self-rewetting fluid droplet evaporation under three different normalized widths of the hydrophilic stripes, namely, $W_{phi}^* = 0.2$, 0.6, and 1.0, are displayed in Fig. 12. From Fig. 12(a) it can be seen that when the normalized hydrophilic stripe width is small ($W_{phi}^* = 0.2$), the droplet is confined in the middle of two hydrophobic stripes so that the spreading of the droplet is restricted, which leads to the normalized evaporation time of $t_e^* > 1$, as seen in Fig. 10(b), indicating that in such a case the evaporation of the self-rewetting fluid droplet on the chemically stripe-patterned surface is much slower than that on a uniformly hydrophilic surface.

When the normalized width of the hydrophilic stripes is increased to $W_{phi}^* = 0.6$, the droplet can spontaneously separate into two small droplets during the evaporation, as shown in Fig. 12(b). The spontaneous separation of the droplet can effectively increase the length of the triple-phase contact line. Accordingly, in comparison with the case of $W_{phi}^* = 0.2$, a significant decrease in the normalized evaporation time can be observed in the case of $W_{phi}^* = 0.6$ [see Fig. 10(b)]. Furthermore, as shown in the middle panel of Fig. 12(b), after the spontaneous separation of the droplet, the two small droplets are elongated in the direction parallel to the stripes due to the confinement effect of the hydrophobic stripes on both sides of the small droplets and this deformation increases the length of the triple-phase contact line to a certain extent, thus increasing the evaporation rate. As a result, the self-rewetting fluid droplet achieves the minimum normalized evaporation time in the case of $W_{phi}^* = 0.6$, which can be viewed as the optimal normalized width of the hydrophilic stripes when $W_{pho}^* = 0.4$. As the normalized hydrophilic stripe width is further

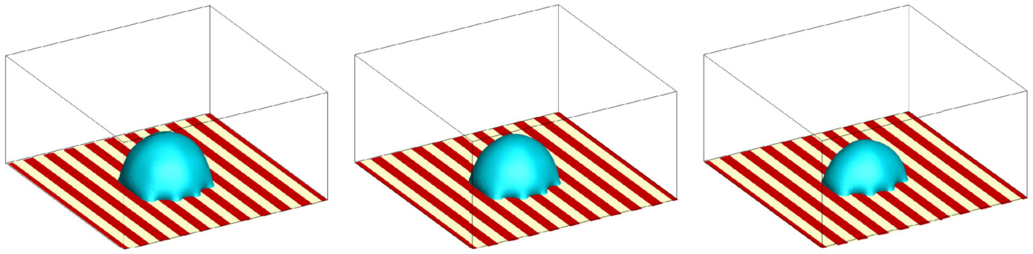

(a) $W_{\text{pho}}^{*} = 0.12$, $W_{\text{phi}}^{*} = 0.12$

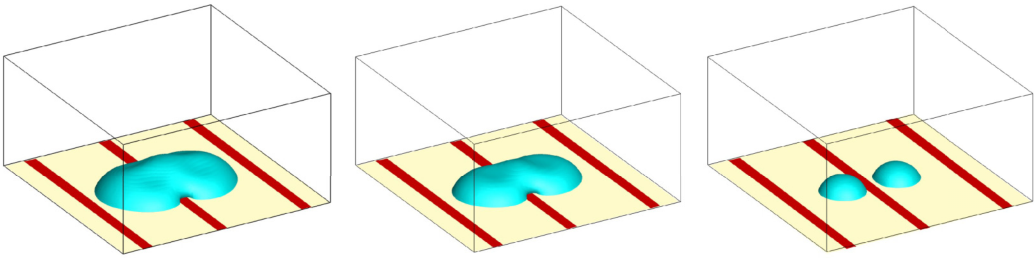

(b) $W_{\text{pho}}^{*} = 0.12$, $W_{\text{phi}}^{*} = 0.8$

FIG. 11. Snapshots of the self-rewetting fluid droplet evaporation on chemically stripe-patterned surfaces in the cases of $W_{\text{pho}}^{*} = 0.12$ with $W_{\text{phi}}^{*} = 0.12$ and 0.8, respectively. From left to right: $t = 7000\delta_t$, $14\,000\delta_t$, and $24\,000\delta_t$, respectively.

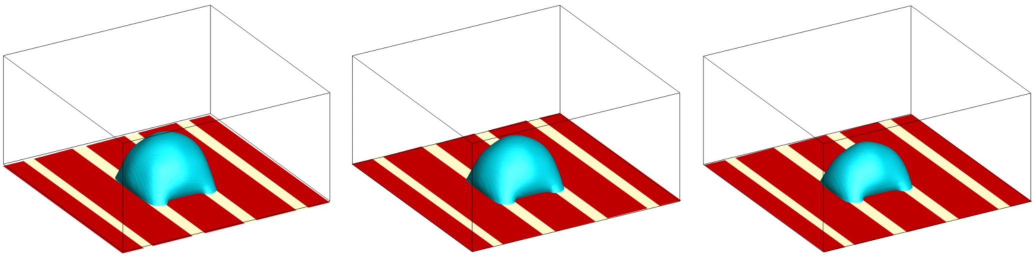

(a) $W_{\text{pho}}^{*} = 0.4$, $W_{\text{phi}}^{*} = 0.2$

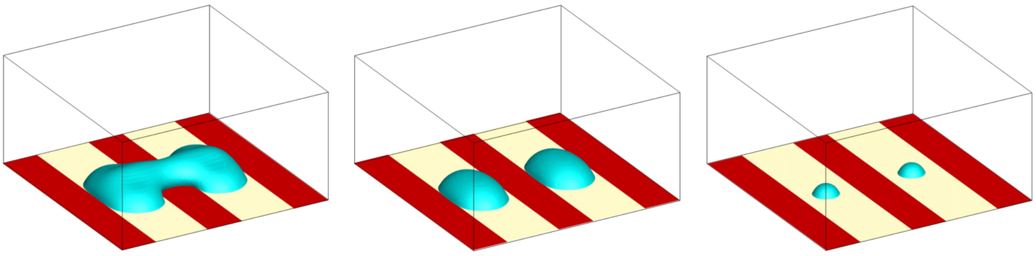

(b) $W_{\text{pho}}^{*} = 0.4$, $W_{\text{phi}}^{*} = 0.6$

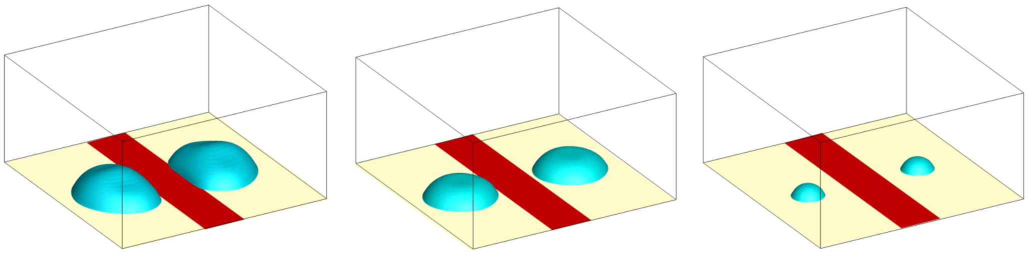

(c) $W_{\text{pho}}^{*} = 0.4$, $W_{\text{phi}}^{*} = 1.0$

FIG. 12. Snapshots of the self-rewetting fluid droplet evaporation on chemically stripe-patterned surfaces in the cases of $W_{\text{pho}}^{*} = 0.4$ with $W_{\text{phi}}^{*} = 0.2$, 0.6, and 1.0, respectively. From left to right: $t = 7000\delta_t$, $t = 14\,000\delta_t$, and $t = 23\,000\delta_t$, respectively.

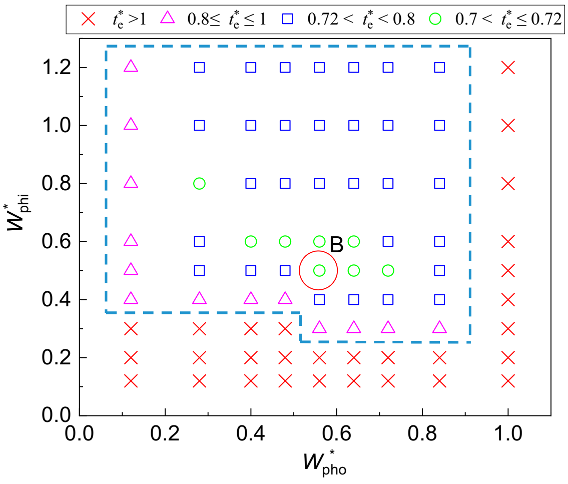

FIG. 13. The effects of the hydrophobic stripe width and the hydrophilic stripe width on the evaporation time of the self-rewetting fluid droplet on the chemically stripe-patterned surfaces. For these 81 cases, the droplet center is initially located at the middle of a hydrophobic stripe.

increased, the hydrophobic stripes on both sides of the droplet have nearly no effect on the evaporation, as seen in Fig. 12(c). The left-hand and middle panels of Fig. 12(b) clearly show that the confinement effect of the hydrophobic stripes on both sides of the droplets elongates the triple-phase contact line. However, there is no such an effect in Fig. 12(c). As a result, the evaporation rate is relatively reduced and the normalized evaporation time of the droplet is slightly increased, as seen in Fig. 10(b). Moreover, by comparing Figs. 12(b) and 12(c) with Fig. 11(b), we can see that the droplet spontaneous separation occurs much earlier in Figs. 12(b) and 12(c) than in Fig. 11(b) owing to the increase of the hydrophilic stripe width, which explains why the cases of Figs. 12(b) and 12(c) yield much lower evaporation time than that of Fig. 11(b).

When the normalized hydrophobic stripe width further increases to $W_{pho}^* = 0.72$, from Fig. 10(c) we can see that the normalized evaporation time t_e^* rapidly decreases with increasing W_{phi}^* and reaches its minimum value in the case of $W_{phi}^* = 0.48$, and then a slight increase is observed in the evaporation time for $W_{phi}^* > 0.48$. Hence, $W_{phi}^* = 0.48$ is the optimal normalized hydrophilic stripe width when the normalized hydrophobic stripe width is taken as $W_{pho}^* = 0.72$. In addition, the dynamic behavior of the self-rewetting fluid droplet in Fig. 10(c) is similar to that in Fig. 10(b), but the minimum value of the normalized evaporation time in Fig. 10(c) is slightly larger than that in Fig. 10(b). Moreover, according to Figs. 10(a)–10(c), we can find that the optimal normalized hydrophilic stripe width, which corresponds to the minimum evaporation time, is gradually decreased as the hydrophobic stripe width increases.

To further illustrate the effects of the hydrophilic stripe width and the hydrophobic stripe width on the evaporation performance of the self-rewetting fluid droplet on the chemically stripe-patterned surfaces, 81 cases are considered by varying the widths of the hydrophilic and hydrophobic stripes. The results of the normalized evaporation time of these cases are displayed in Fig. 13. The 81 cases can be classified into four groups based on the normalized evaporation time of the droplet. As shown in Fig. 13, when W_{pho}^* is close to 1.0 or $W_{phi}^* \leqslant 0.3$, the normalized evaporation time is basically

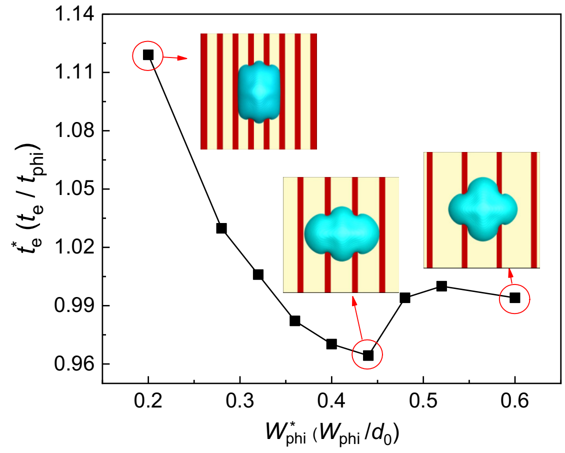

(a) $W_{pho}^* = 0.12$

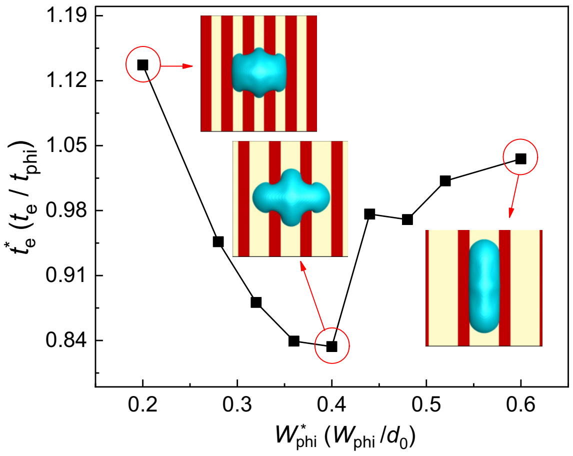

(b) $W_{pho}^* = 0.24$

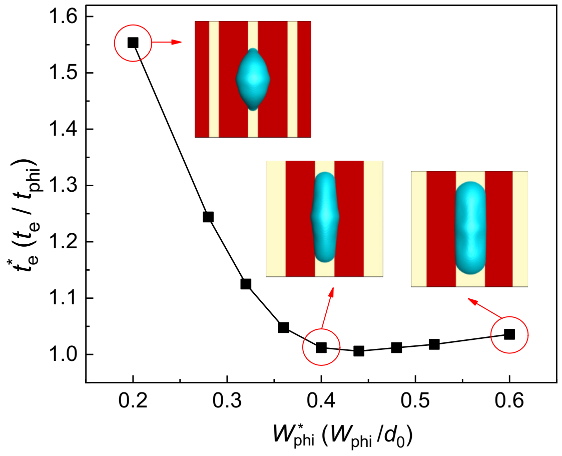

(c) $W_{pho}^* = 0.6$

FIG. 14. Variations of the normalized evaporation time t_e^* with the normalized hydrophilic stripe width W_{phi}^* when the normalized hydrophobic stripe width is taken as $W_{pho}^* = 0.12$, 0.24, and 0.6, respectively. For these cases, the droplet center is initially located at the middle of a hydrophilic stripe. The snapshots shown in this figure are also taken at $t = 6000\delta_t$.

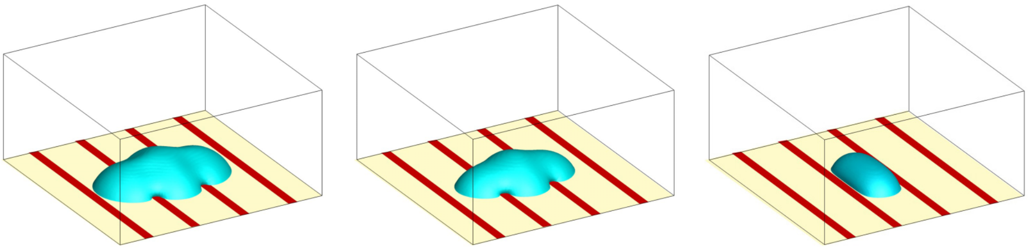

FIG. 15. Snapshots of the self-rewetting fluid droplet evaporation on the chemically stripe-patterned surfaces in the case of $W^*_{\mathrm{pho}} = 0.12$ and $W^*_{\mathrm{phi}} = 0.44$ with the droplet center being initially located at the middle of a hydrophilic stripe. From left to right: $t = 7000\delta_t$, $140\,00\delta_t$, and $230\,00\delta_t$, respectively.

larger than 1.0 because the spreading of the droplet is restricted and no droplet separation occurs in the cases of this group. For the cases marked with the triangles, the spreading space of the droplet becomes larger and in some cases of this group the droplet can spontaneously separate into two small droplets, although the separation may occur at the late stage of the evaporation, which elongates the triple-phase contact line and leads to a decrease of the normalized evaporation time in comparison with the cases of the first group. Furthermore, in all the cases of $0.28 \leqslant W^*_{\mathrm{pho}} \leqslant 0.84$ and $W^*_{\mathrm{phi}} > 0.4$, the self-rewetting fluid droplet can spontaneously separate into two small droplets during the evaporation and therefore achieve a higher evaporation rate. Moreover, the cases represented by the circles fall into the fourth group (also the best group), which not only ensures the spontaneous separation of the self-rewetting fluid droplet but also elongates the contact line length of the small droplets after the droplet separation, thus providing a very low normalized evaporation time of $0.7 < t^*_e \leqslant 0.72$. Specifically, the lowest normalized evaporation time ($t^*_e \approx 0.702$) is achieved in the case of $W^*_{\mathrm{pho}} = 0.56$ and $W^*_{\mathrm{phi}} = 0.5$, namely, the case denoted by point B in Fig. 13.

C. Evaporation performance and dynamic behavior of self-rewetting fluid droplets on chemically patterned surfaces when the droplet center is located at the middle of a hydrophilic stripe

In this section, we turn our attention to the cases in which the droplet center is initially located at the middle of a hydrophilic stripe. The simulation parameters are basically the same as those used in the previous section except for the adjustment of the initial location of the self-rewetting fluid droplet on the chemically stripe-patterned surfaces. Figure 14 displays the variation of the normalized evaporation time t^*_e of the self-rewetting fluid droplet with the normalized hydrophilic stripe width W^*_{phi} under three different widths of the hydrophobic stripes. From the figure we can see that that the variation of the normalized evaporation time shows a similar trend when the normalized hydrophobic stripe width is taken as $W^*_{\mathrm{pho}} = 0.12$ and 0.24. Specifically, Figs. 14(a) and 14(b) show that the normalized evaporation time t^*_e decreases rapidly with increasing W^*_{phi} until it reaches a minimum value smaller than 1.0, and then the normalized evaporation time basically increases with the increase of W^*_{phi}. However, for the cases of $W^*_{\mathrm{pho}} = 0.6$, the normalized evaporation time is always larger than 1.0 [see Fig. 14(c)] regardless of the choice of the hydrophilic stripe width, although the variation of the normalized evaporation time also exhibits a trend of first decreasing and then increasing after reaching its minimum value.

For the cases of $W^*_{\mathrm{pho}} = 0.12$, when the hydrophobic and hydrophilic stripe widths are both much smaller than the initial droplet diameter, the evaporation dynamics of the self-rewetting fluid droplet is similar to that of the cases in which the droplet center is initially located at the middle of a hydrophobic stripe. From the left-hand snapshot in Fig. 14(a), we can see that in the case of $W^*_{\mathrm{pho}} = 0.12$ and $W^*_{\mathrm{phi}} = 0.2$ the spreading of the droplet is restricted due to the confinement effect of the hydrophobic stripes on the two sides of the droplet. Correspondingly, the normalized evaporation time is larger than 1.0, indicating that the droplet evaporation in this case is slower than that on a uniformly hydrophilic surface. As the width of the hydrophilic stripes increases, the spreading space can be enlarged as shown in Fig. 15 for the case of $W^*_{\mathrm{pho}} = 0.12$ and $W^*_{\mathrm{phi}} = 0.44$, from which we can see that the droplet is elongated in the direction perpendicular to the stripes during the main evaporation process. Meanwhile, the shrinking of the triple-phase contact line on the hydrophobic stripes can be observed in Fig. 15. However, in such a case the hydrophobic stripes are too narrow to support the spontaneous separation of the self-rewetting droplet. As a result, the normalized evaporation time is still very close to 1.0, as seen in Fig. 14(a). When the hydrophilic stripe width is further increased, the elongation of the droplet in the direction perpendicular to the stripes becomes gradually weaker, which can be observed by comparing the middle and the right-hand snapshots in Fig. 14(a). Accordingly, the evaporation rate is reduced to a certain extent and a slight increase can be observed in the normalized evaporation time.

Figure 16 displays some snapshots of the self-rewetting fluid droplet evaporation in the cases of $W^*_{\mathrm{pho}} = 0.24$ with three different normalized widths of the hydrophilic stripes. When the normalized hydrophilic stripe width is relatively small ($W^*_{\mathrm{phi}} = 0.2$), the pinning phenomenon of the contact line can be observed in Fig. 16(a) in the direction perpendicular to the stripes, while in the direction parallel to the stripes the contact line shrinks on the surface. These phenomena are similar to those shown in Fig. 11(a). As the hydrophilic stripe width is further increased to $W^*_{\mathrm{phi}} = 0.4$, the spreading space is enlarged for the droplet. Owing to the droplet spreading on the hydrophilic stripes and the droplet shrinking on the hydrophobic stripes, two liquid bridges can be found in the middle panel of Fig. 16(b). As the evaporation proceeds, the two liquid bridges become narrower and narrower, and finally

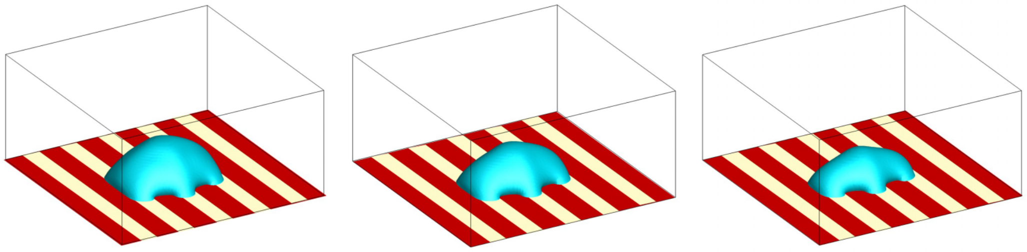

(a) $W^*_{\text{pho}} = 0.24$, $W^*_{\text{phi}} = 0.2$

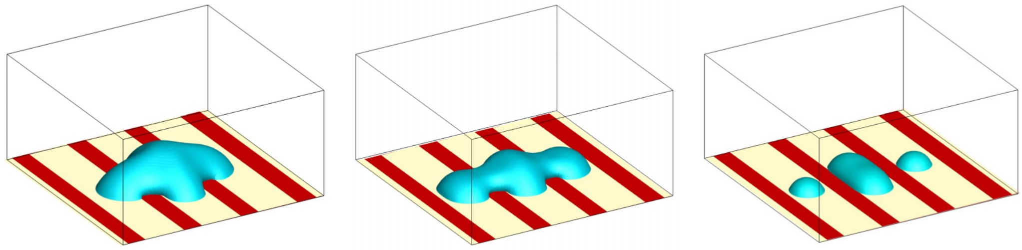

(b) $W^*_{\text{pho}} = 0.24$, $W^*_{\text{phi}} = 0.4$

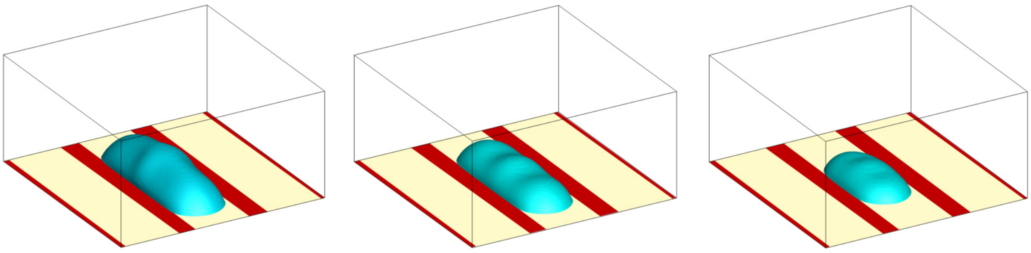

(c) $W^*_{\text{pho}} = 0.24$, $W^*_{\text{phi}} = 0.6$

FIG. 16. Snapshots of the self-rewetting fluid droplet evaporation on the chemically stripe-patterned surfaces in the cases of $W^*_{\text{pho}} = 0.24$ with $W^*_{\text{phi}} = 0.2$, 0.4, and 0.5, respectively. For these cases, the droplet center is initially located at the middle of a hydrophilic stripe. From left to right: $t = 5000\delta_t$, $130\,00\delta_t$, and $200\,00\delta_t$, respectively.

break, which causes the droplet to be separated into three small droplets, as shown in the right-hand panel of Fig. 16(b). Due to the spontaneous separation behavior of the droplet, the evaporation rate is enhanced and the normalized evaporation time of the droplet is considerably reduced as compared with other cases [see Fig. 14(b)].

Note that, although the droplet can spontaneously separate into three small droplets in the case of $W^*_{\text{pho}} = 0.24$ and $W^*_{\text{phi}} = 0.4$, its normalized evaporation time ($t^*_{\text{e}} \approx 0.833$) is relatively larger than that of the case shown in Fig. 12(c), in which the droplet separates into two small droplets during the evaporation. This is because the droplet separation occurs much earlier in the case shown in Fig. 12(c) than that in Fig. 16(b). When the width of the hydrophilic stripes further increases, the edge of the droplet in the x direction is initially located at the two hydrophobic stripes near the central hydrophilic stripe. During the evaporation process, the droplet rapidly shrinks toward the central hydrophilic stripe in the x direction and is elongated on the central hydrophilic stripe in the y direction, like a liquid finger, as shown in Fig. 16(c). In other words, in the case of $W^*_{\text{pho}} = 0.24$ and $W^*_{\text{phi}} = 0.6$ the evaporation of the droplet mainly occurs on the central hydrophilic stripe. As a result, the normalized evaporation time is significantly increased in comparison with the cases of $W^*_{\text{pho}} = 0.24$ and $W^*_{\text{phi}} = 0.4$, as seen in Fig. 14(b). Furthermore, for the cases displayed in Fig. 14(c) with relatively large widths of the hydrophilic stripes, the droplet dynamics is similar to that shown in Fig. 16(c). Correspondingly, the normalized evaporation time of these cases is also larger than 1.0.

In this section we have also simulated 81 cases so as to clearly illustrate the influences of the hydrophilic stripe width and the hydrophobic stripe width on the evaporation time of the self-rewetting fluid droplet on the chemically stripe-patterned surfaces with the droplet center being initially located at the middle of a hydrophilic stripe. The results are summarized in Fig. 17, in which the investigated cases can be classified into three groups according to the evaporation time of the droplet. By comparing Fig. 17 with Fig. 14, we can see that in Fig. 17 the region that corresponds to $t^*_{\text{e}} \leqslant 1$ is much narrower as compared with that in Fig. 14. Particularly, it can be seen that, when $W^*_{\text{pho}} > 0.3$, all the cases lead to $t^*_{\text{e}} > 1$. This is mainly because, for the cases with the droplet center being initially located at the middle of a hydrophilic stripe, the droplet will rapidly shrink toward the central hydrophilic stripe when the hydrophobic stripe width

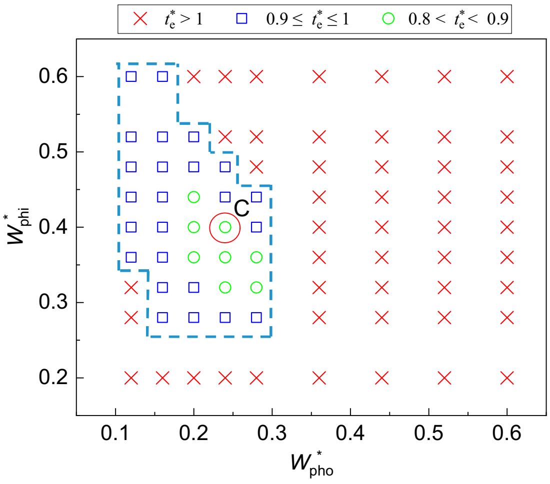

FIG. 17. The effects of the hydrophobic stripe width and the hydrophilic stripe width on the evaporation time of the self-rewetting fluid droplet on the chemically stripe-patterned surfaces. For these 81 cases, the droplet center is initially located at the middle of a hydrophilic stripe.

is relatively large, and then the droplet will be concentrated on the central hydrophilic stripe during the evaporation. The cases denoted by the squares yield the normalized evaporation time of $0.9 \leqslant t_e^* \leqslant 1$, while the circles represent the best group which corresponds to the normalized evaporation time of $0.8 < t_e^* < 0.9$ resulting from the spontaneous separation of the self-rewetting fluid droplet into three small droplets during the evaporation. In addition, the lowest normalized evaporation time is achieved in the case denoted by point C in Fig. 17.

IV. CONCLUSIONS

In this paper, we have numerically investigated the evaporation performance and the dynamic behavior of self-rewetting fluid droplets on chemically stripe-patterned surfaces using a thermal multiphase LB model with liquid-vapor phase change. First, the different dynamic behaviors of a self-rewetting fluid droplet and a conventional fluid droplet during their evaporation on a hydrophilic surface with a hydrophobic stripe were studied and the associated separation mechanism was explored. It is found that the self-rewetting fluid droplet can spontaneously separate into two droplets during its evaporation on the hydrophilic surface with a hydrophobic stripe, while no separation occurs during the evaporation of the conventional fluid droplet. The spontaneous separation of the self-rewetting fluid droplet during the evaporation is found to be caused by two factors, i.e., the spreading of the droplet on the hydrophilic region and the shrinking of the droplet on the hydrophobic stripe. The positive surface tension gradient of the self-rewetting fluid droplet results in a favorable unbalanced Young's force, which not only promotes its spreading on the hydrophilic region but also promotes its shrinking on the hydrophobic stripe. However, the negative surface tension gradient of the conventional fluid droplet prevents it from shrinking on the hydrophobic stripe and spreading on the hydrophilic region, which suppresses the appearance of the spontaneous separation during evaporation.

Then, by varying the widths of the hydrophilic and hydrophobic stripes as well as the initial location of the droplet, we have explored the evaporation mechanism of self-rewetting fluid droplets on chemically stripe-patterned surfaces. It is found that both the stripe width and the initial location of the droplet have significant influence on the dynamic behavior and the evaporation efficiency of the self-rewetting fluid droplet. For different relative positions between the droplet and the stripes, the droplet may spontaneously separate into two or three droplets when the stripe width is within an optimal range. Correspondingly, the evaporation time can be significantly reduced as the separation of the self-rewetting fluid droplet can effectively increase the length of the triple-phase contact line and enhance the evaporation heat transfer. When the droplet is initially located at the middle of a hydrophobic stripe, the spontaneous separation is found in all the cases of $0.28 \leqslant W_{\text{pho}}^* \leqslant 0.84$ and $W_{\text{phi}}^* > 0.4$. However, when the droplet is initially located at the middle of a hydrophilic stripe, there are only a few cases that can lead to spontaneous separation. We believe that the present study would be useful for understanding the evaporation characteristics of self-rewetting fluid droplets on chemically patterned surfaces. In future work, attention will be paid to some more complex surfaces, such as patterned surfaces with cross stripes.

ACKNOWLEDGMENT

This work was supported by the National Natural Science Foundation of China (Grants No. 52176093 and No. 51822606).

---

[1] T. Furuta, M. Sakai, T. Isobe, and A. Nakajima, Evaporation behavior of microliter-and sub-nanoliter-scale water droplets on two different fluoroalkylsilane coatings, Langmuir **25**, 11998 (2009).

[2] E. L. Talbot, L. Yang, A. Berson, and C. D. Bain, Control of the particle distribution in inkjet printing through an evaporation-driven sol–gel transition, ACS Appl. Mater. Interfaces **6**, 9572 (2014).

[3] F. Salata and M. Coppi, A first approach study on the desalination of sea water using heat transformers powered by solar ponds, Appl. Energy **136**, 611 (2014).

[4] W.-L. Cheng, W.-W. Zhang, H. Chen, and L. Hu, Spray cooling and flash evaporation cooling: The current development and application, Renewable Sustainable Energy Rev. **55**, 614 (2016).

[5] H. Hu and R. G. Larson, Evaporation of a sessile droplet on a substrate, J. Phys. Chem. B **106**, 1334 (2002).

[6] A.-M. Cazabat and G. Guena, Evaporation of macroscopic sessile droplets, Soft Matter **6**, 2591 (2010).

[7] H. Y. Erbil, Evaporation of pure liquid sessile and spherical suspended drops: A review, Adv. Colloid Interface Sci. **170**, 67 (2012).

[8] N. Kovalchuk, A. Trybala, and V. Starov, Evaporation of sessile droplets, Curr. Opin. Colloid Interface Sci. **19**, 336 (2014).

[9] H. P. Jansen, O. Bliznyuk, E. S. Kooij, B. Poelsema, and H. J. Zandvliet, Simulating anisotropic droplet shapes on chemically striped patterned surfaces, Langmuir **28**, 499 (2012).

[10] H. P. Jansen, K. Sotthewes, C. Ganser, C. Teichert, H. J. Zandvliet, and E. S. Kooij, Tuning kinetics to control droplet shapes on chemically striped patterned surfaces, Langmuir **28**, 13137 (2012).

[11] Y. Yu, Q. Li, C. Q. Zhou, P. Zhou, and H. J. Yan, Investigation of droplet evaporation on heterogeneous surfaces using a three-dimensional thermal multiphase lattice Boltzmann model, Appl. Therm. Eng. **127**, 1346 (2017).

[12] B. Dong, F. Wang, X. Zhang, and X. Jiang, 3D lattice Boltzmann simulation of droplet evaporation on patterned surfaces: Study of pinning–depinning mechanism, Int. J. Multiphase Flow **125**, 103218 (2020).

[13] O. Bliznyuk, E. Vereshchagina, E. S. Kooij, and B. Poelsema, Scaling of anisotropic droplet shapes on chemically stripe-patterned surfaces, Phys. Rev. E **79**, 041601 (2009).

[14] O. Bliznyuk, H. P. Jansen, E. S. Kooij, and B. Poelsema, Initial spreading kinetics of high-viscosity droplets on anisotropic surfaces, Langmuir **26**, 6328 (2010).

[15] H. P. Jansen, H. J. W. Zandvliet, and E. S. Kooij, Evaporation of elongated droplets on chemically stripe-patterned surfaces, Int. J. Heat Mass Transfer **82**, 537 (2015).

[16] Q. Li, P. Zhou, and H. J. Yan, Pinning-depinning mechanism of the contact line during evaporation on chemically patterned surfaces: A lattice Boltzmann study, Langmuir **32**, 9389 (2016).

[17] Y. Abe, A. Iwaski, and K. Tanaka, Thermal management with self-rewetting fluids, Microgravity Sci. Technol. **16**, 148 (2005).

[18] R. Vochten and G. Petre, Study of the heat of reversible adsorption at the air-solution interface. II. Experimental determination of the heat of reversible adsorption of some alcohols, J. Colloid Interface Sci. **42**, 320 (1973).

[19] R. Savino, A. Cecere, and R. Di Paola, Surface tension-driven flow in wickless heat pipes with self-rewetting fluids, Int. J. Heat Fluid Flow **30**, 380 (2009).

[20] Y. Hu, K. Huang, and J. Huang, A review of boiling heat transfer and heat pipes behaviour with self-rewetting fluids, Int. J. Heat Mass Transfer **121**, 107 (2018).

[21] A. Sitar and I. Golobic, Heat transfer enhancement of self-rewetting aqueous n-butanol solutions boiling in microchannels, Int. J. Heat Mass Transfer **81**, 198 (2015).

[22] S. Tsang, Z.-H. Wu, C.-H. Lin, and C.-l. Sun, On the evaporative spray cooling with a self-rewetting fluid: Chasing the heat, Appl. Therm. Eng. **132**, 196 (2018).

[23] E. Lim, T. C. Kueh, and Y. M. Hung, Inverse-thermocapillary evaporation in a thin liquid film of self-rewetting fluid, Int. J. Numer. Methods Heat Fluid Flow **31**, 1124 (2020).

[24] Y. Yang, L. Zhou, X. Du, and Y. Yang, Fluid flow and thin-film evolution near the triple line during droplet evaporation of self-rewetting fluids, Langmuir **34**, 3853 (2018).

[25] K. Sefiane, X. Yu, G. Duursma, and J. Xu, On heat and mass transfer using evaporating self-rewetting mixtures in microchannels, Appl. Therm. Eng. **179**, 115662 (2020).

[26] S. Chen and G. D. Doolen, Lattice Boltzmann method for fluid flows, Annu. Rev. Fluid Mech. **30**, 329 (1998).

[27] C. K. Aidun and J. R. Clausen, Lattice-Boltzmann method for complex flows, Annu. Rev. Fluid Mech. **42**, 439 (2010).

[28] Q. Li, K. H. Luo, Q. Kang, Y. He, Q. Chen, and Q. Liu, Lattice Boltzmann methods for multiphase flow and phase-change heat transfer, Prog. Energy Combust. Sci. **52**, 62 (2016).

[29] A. Xu, W. Shyy, and T. Zhao, Lattice Boltzmann modeling of transport phenomena in fuel cells and flow batteries, Acta Mech. Sin. **33**, 555 (2017).

[30] D. Sun, M. Zhu, S. Pan, and D. Raabe, Lattice Boltzmann modeling of dendritic growth in a forced melt convection, Acta Mater. **57**, 1755 (2009).

[31] H. Huang, M. Sukop, and X. Lu, *Multiphase Lattice Boltzmann Methods: Theory and Application* (John Wiley & Sons, New York, 2015).

[32] Q. Li and K. H. Luo, Achieving tunable surface tension in the pseudopotential lattice Boltzmann modeling of multiphase flows, Phys. Rev. E **88**, 053307 (2013).

[33] Q. Li, K. H. Luo, and X. J. Li, Lattice Boltzmann modeling of multiphase flows at large density ratio with an improved pseudopotential model, Phys. Rev. E **87**, 053301 (2013).

[34] A. Xu, T. Zhao, L. An, and L. Shi, A three-dimensional pseudo-potential-based lattice Boltzmann model for multiphase flows with large density ratio and variable surface tension, Int. J. Heat Fluid Flow **56**, 261 (2015).

[35] L. Fei, J. Du, K. H. Luo, S. Succi, M. Lauricella, A. Montessori, and Q. Wang, Modeling realistic multiphase flows using a non-orthogonal multiple-relaxation-time lattice Boltzmann method, Phys. Fluids **31**, 042105 (2019).

[36] A. Montessori, P. Prestininzi, M. La Rocca, and S. Succi, Entropic lattice pseudo-potentials for multiphase flow simulations at high Weber and Reynolds numbers, Phys. Fluids **29**, 092103 (2017).

[37] S. P. Thampi, S. Ansumali, R. Adhikari, and S. Succi, Isotropic discrete Laplacian operators from lattice hydrodynamics, J. Comput. Phys. **234**, 1 (2013).

[38] M. Sbragaglia, R. Benzi, L. Biferale, S. Succi, K. Sugiyama, and F. Toschi, Generalized lattice Boltzmann method with multirange pseudopotential, Phys. Rev. E **75**, 026702 (2007).

[39] R. Savino, A. Cecere, R. Di Paola, Y. Abe, D. Castagnolo, and R. Fortezza, Marangoni heat pipe: An experiment on board MIOsat Italian microsatellite, Acta Astronaut. **65**, 1582 (2009).

[40] A. Marchand, J. H. Weijs, J. H. Snoeijer, and B. Andreotti, Why is surface tension a force parallel to the interface? Am. J. Phys. **79**, 999 (2011).